

See discussions, stats, and author profiles for this publication at: <https://www.researchgate.net/publication/269467115>

Molecular Dynamics Simulations of Heart-type Fatty Acid Binding Protein in Apo and Holo Forms, and Hydration Structure Analyses in the Binding Cavity

ARTICLE *in* THE JOURNAL OF PHYSICAL CHEMISTRY B · DECEMBER 2014

Impact Factor: 3.3 · DOI: 10.1021/jp510384f · Source: PubMed

CITATIONS

2

READS

18

4 AUTHORS, INCLUDING:



Michio Murata

Osaka University

224 PUBLICATIONS 7,330 CITATIONS

[SEE PROFILE](#)



Shigeru Matsuoka

Osaka University

59 PUBLICATIONS 959 CITATIONS

[SEE PROFILE](#)

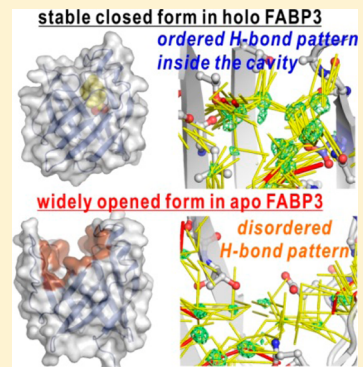
Molecular Dynamics Simulations of Heart-type Fatty Acid Binding Protein in Apo and Holo Forms, and Hydration Structure Analyses in the Binding Cavity

Daisuke Matsuoka,^{†,‡,§} Shigeru Sugiyama,^{†,‡} Michio Murata,^{*,†,‡,§} and Shigeru Matsuoka^{*,†,‡,§}

[†]JST ERATO, Lipid Active Structure Project, [‡]Department of Chemistry, Graduate School of Science, and [§]Project Research Center for Fundamental Science, Osaka University, 1-1 Machikaneyama, Toyonaka, Osaka 560-0043, Japan

Supporting Information

ABSTRACT: Intracellular lipid binding proteins (iLBPs) share distinctive features: a rigid protein structure composed of a β -barrel and an α -helix cap, and a large internalized water cluster. Although X-ray crystallographic studies have elucidated the three-dimensional structures of iLBPs, the protein dynamics and the role of the large water cluster in protein function remain unknown. In the present study, we performed molecular dynamics (MD) simulations on human heart-type fatty acid binding protein (FABP3), a typical iLBP that is highly expressed in heart and skeletal muscles, and showed that an altered mode of protein dynamics and rearrangement of the internal water cluster are key elements of ligand binding. Using simulations without a ligand at 310 K, we first demonstrated that FABP3 adopts a wide-open conformation, achieved by a combination of two modes of dynamics: portal opening by a domain motion of the α -helices and gap opening by cleavage of the hydrogen-bond network between β D and β E strands. In contrast, stearic acid-bound FABP3 mainly adopted a closed form, stabilized by the H-bond network inside the binding cavity, which latches the gap, and by protein–ligand hydrophobic interactions. The wide-open apo FABP3 represents a biologically important conformation relevant to ligand loading.



1. INTRODUCTION

Heart-type fatty acid binding protein (FABP3) is a member of the intracellular lipid binding protein (iLBP) family, which is abundant in heart and skeletal muscle. This protein is thought to be involved in fatty acid uptake, transport, and metabolism,^{1–7} especially delivery of long-chain fatty acids (LCFAs) from the inner plasma membrane to the mitochondria for β -oxidization via the collision model.^{1,3,8–11} The three-dimensional (3D) structure of FABP3 has been determined by X-ray crystallography and solution nuclear magnetic resonance (NMR) spectroscopy.^{12–16} It is composed of a pair of five-stranded antiparallel β -sheets (β A– β J) capped with two short α -helices (α I and α II) forming a large interior cavity that can accommodate a single LFA molecule (Figure 1). The adjacent antiparallel β -strands, β D and β E, are not within H-bond distance and the space between them is referred to as the “gap”. In the binding cavity, a bound LFA is folded in a U-shaped conformation and anchored at one of the oxygen atoms of the carboxyl group by the side chains of R126 and Y128. The alkyl chain of the bound LFA contacts the hydrophobic residues lining the cavity, most of which are located on α II and the C–D and E–F loops.^{12–14,16,17} Proteins in the FABP subfamily IV, including FABP3, FABP4, FABP5, FABP7, and FABP8, share this β -barrel structure and the FA-binding mode (Figure S1 in Supporting Information).^{5,18–22}

In crystal structures of the human FABP3–stearic acid (STE) complex, the binding cavity contains 13 well-ordered water molecules that form an extensive H-bond network, along with

polar protein atoms lining the cavity.^{13,23} The network connects the gap and the FA carboxyl moiety, and also surrounds the hydrophobic FA alkyl chain (Figure 1). Because this well-ordered water cluster is a common feature of the FABP subfamily IV,^{19–23} these water molecules are thought to be indispensable for protein structure stabilization and to be involved in ligand recognition, similar to those located in protein interiors or clefts, or interfaces of protein–protein complexes.^{24–29}

Small conformational variations among the protein crystal structures deposited in Protein Data Bank (PDB) may indicate another remarkable feature of this protein subfamily.^{5,30} These proteins bind not only LCFA but also hydrophobic small molecules, such as 1-anilinonaphthalene-8-sulfonic acid (ANS)^{15,31} or carbazole derivatives,^{7,32,33} but their crystal structures are little different from each other. The apo protein crystal structures in this subfamily also usually show closed conformations, similar to those of the holo forms.^{3,34,35} In these surprisingly similar protein structures, the internalized binding cavities are not in clear contact with the external environments. From these static structures, it is difficult to predict how a FA enters and leaves the FABP3 binding site; this is fundamental to understanding the molecular mechanism of ligand selection and delivery in FABP3. The portal that controls external ligands’

Received: October 15, 2014

Revised: December 2, 2014

Published: December 8, 2014



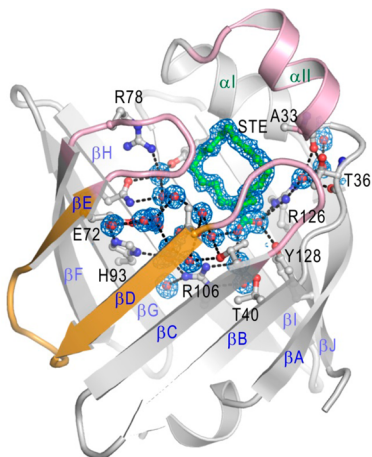


Figure 1. Protein structure of FABP3, showing a bound STE and the internal water molecules (PDB accession code: 4WBK). The gray cartoon model shows the protein, the green stick model shows the bound STE, and the red spheres show the water molecules. The portal and gap regions are shown in pink and orange, respectively. The blue mesh shows the omit map of the internal water molecules and bound STE, and the contour level is 3.0σ . Putative H-bonds are shown by broken black lines.

access to the binding cavity has thus attracted considerable interest in the past two decades, but it remains elusive.^{2,36}

Based on the structural analyses in crystal and in solution, the α II, C–D, and E–F loops have been proposed to constitute the portal, based on their dynamic properties.^{2,3,35–38} This hypothesis has been supported by a database analysis³⁹ and a mutagenesis study.⁴⁰ Friedman et al. carried out a further examination of the proposed portal using 4–13 ns MD simulations at 300 K, in which palmitic acid (PLM) was initially positioned outside of apo FABP2/4.^{41,42} However, in these simulations, the FA could not enter the binding site without any artifacts. On the other hand, when they simulated the ligand binding process of apo toad liver basic FABP (Lb-FABP), a single PLM molecule successfully reached the putative inner binding site.⁴³ The primary difference between these simulations was the initial conformation of the ligand-free crystal structure: apo FABP2/4 adopted a closed conformation, but apo Lb-FABP showed an open-portal conformation.⁴⁴ Although Lb-FABP and FABP1/6 are functionally and structurally distinct from proteins in the FABP subfamily IV,^{3,5,7,18,44–47} these results strongly suggest that elucidating open conformations is essential for understanding the mechanism underlying ligand binding to FABP. Recently, murine cellular retinoic acid binding protein 1 (CRABP-1) has been suggested to have more dynamic features in the apo form, which results in a population shift to the open state at low concentrations of urea.⁴⁷ Because CRABP-1 is a member of iLBP, it is expected that perturbative approaches will allow FABP3 to show more dynamic features and adopt an open conformation in solution.

In the present study, we performed MD simulations comparing the apo and STE-bound forms of FABP3 and present the first report of open conformations of FABP3 in the apo form. First, we examined whether FABP3 shows an open conformation in MD simulations at 310 K over 150 ns; we applied higher temperatures and longer simulation times than previous MD studies reporting closed apo structures.^{17,22,41,42,48,49} The STE-bound form of the protein showed

a closed conformation in most snapshots, but the apo protein predominantly displayed the open conformation. Next, to investigate the role of the internal water molecules in determining protein conformation, we investigated the hydration distribution density, time-averaged H-bond patterns, and the interactions dynamics between the internal water molecules and polar protein atoms. These analyses demonstrated that water molecules inside the cavity reside at defined hydration sites and that coherent H-bond patterns are formed in the ligand-bound form. On the other hand, in the apo form, internal water molecules are more mobile, and the H-bonds show a disordered pattern. Through the hydration structure analyses of the binding cavity, we explored the relationships among the protein, bound FA, and internal water molecules, and investigated the role of the gap in protein conformation selection. Based on these results, we propose a novel molecular mechanism underlying the FA loading process in FABP3.

2. COMPUTATIONAL DETAILS

2.1. Molecular Dynamics Simulation. **2.1.1. Simulation of Human STE-Bound FABP3.** The crystal structure of the FABP3–STE complex at cryogenic temperature was solved at 1.37 Å resolution in our laboratory (PDB accession code: 4WBK). The initial structure for use in the MD simulations was taken from the final stage of the crystal structure refinement. The bound STE was modeled in a deprotonated state, according to pK_a values estimated by the program PROPKA 3.1.⁵⁰ The protein, bound STE, and crystal water molecules were immersed in a water box, and 2 Na^+ ions were added in bulk solution to neutralize the simulation system under periodic boundary conditions. A solvent box extended at least 12.0 Å from the protein surface. As the result, the initial dimensions of the box were 69.19 Å × 69.19 Å × 69.19 Å, and it contained 9962 water molecules and a total of 32035 atoms. Two simulations were run using the same initial coordinates and different initial velocities. Here, we refer to the two runs as STE_NPT_run1 and STE_NPT_run2, respectively.

All simulations were performed using the program MARBLE⁵¹ and using CHARMM36/CMAP for protein,⁵² CHARMM36 for STE,⁵³ and TIP3P for water molecules⁵⁴ as the force-field parameters. To control the temperature and the pressure of the systems, the extended-system approach proposed by Martyna et al. was used.⁵⁶ The Nosé–Hoover thermostat chain length was five. Electrostatic interactions were calculated using the particle mesh Ewald method. The Lennard-Jones potential was smoothly switched to zero over the range of 8–10 Å. The symplectic integrator for rigid bodies was used with a time step of 2 fs, in which water and the $\text{CH}_x \text{NH}_x$ ($x = 1, 2, 3$), SH, and OH groups were treated as rigid bodies.

After an energy minimization of 2000 steps for the whole system, the system was gradually heated to 310.15 K for 100 ps under an NPT ensemble with constraints on the positions of all heavy atoms except solvent atoms. The harmonic force constant of the constraints was 1 kcal/(mol·Å²). Subsequently, an MD simulation was performed for 100 ps under the NPT ensemble, using the same constraints. Next, the constraints were gradually decreased over a period of 150 ps, and an additional equilibration run was performed over a period of 650 ps with no constraints. After equilibration, 150 ns production runs were performed at 1 atm and 310.15 K. The coordinates were saved every 1.0 ps for performing subsequent calculations. Accessible surface area (ASA) values were also calculated, using the method proposed by Lee and Richards, for every

snapshot.⁵⁵ For calculation of ASA, all water molecules and hydrogen atoms in both the protein and STE were ignored.

The protein molecules in all the snapshots were superimposed on the energy-minimized structure, using the method proposed by Kabsch.^{57,58} With the operation of the superimposition, all water molecules, ions, and bound STE molecules were simultaneously translated and rotated.

2.1.2. Simulation of the Apo Form of Human FABP3. The initial structure of the apo form of human FABP3 was obtained by simply removing the bound STE from the 1.37 Å resolution crystal structure. The STE in the binding cavity was replaced with water molecules. We first placed water molecules at the hydration sites of polar protein atoms predicted by the program DM_hydra.⁵⁹ Then, water molecules were added manually, with consideration for the tetrahedral H-bond geometry of water molecules.^{60,61}

Following whole-system energy minimization of 2000 steps, the system was gradually heated to 310.15 K for 100 ps under an *NPT* ensemble, and then a simulation was performed for 1400 ps under the *NPT* ensemble, using the same constraints employed for the STE-bound form. In the subsequent simulation, the harmonic force constants were weakened from 1.0 kcal/(mol·Å²) to 0.10 kcal/(mol·Å²) over 1300 ps. With the very weak positional constraints applied to the protein heavy atoms, the manually placed internal water molecules were fully relaxed and equilibrated over a period of 6000 ps. Then the constraints were removed over 200 ps, and an additional equilibration run of 1000 ps was performed with no constraints. After the equilibration, 210 ns production runs were performed at 1 atm and 310.15 K.

The parameters and conditions used were identical to those used for the STE-bound form, except the box dimensions and initial velocities. We ran two simulations for the apo form, with different box dimensions. For the first run (apo_NPT_run1), the initial box dimensions were 69.18 Å × 69.18 Å × 69.18 Å and extended at least 12.0 Å from the protein surface. The box contained 9980 water molecules, and the total number of atoms was 32 034. Large structural changes of the protein molecules were observed in the first run, and so for the second run (apo_NPT_run2) we used a larger box with dimensions of 75.19 Å × 75.19 Å × 75.19 Å, extending at least 15.0 Å from the protein surface. However, we found that the difference in box dimensions made little difference in the results of the two simulations (Figure 2). For the second run, the box contained 13 010 water molecules and a total of 41 123 atoms.

2.2. Calculation of Distribution Density and ccHB Pattern inside the Binding Cavity. To examine the hydration structures in the binding cavity of FABP3, we calculated the hydration distribution density and time-averaged H-bond patterns. For this purpose, we performed another 5.0 ns MD simulations under *NVT* conditions at 310.15 K, whose initial structures were taken from snapshots in STE_NPT_run1 and apo_NPT_run1 (Table 1). The coordinates were saved every 50 fs.

In the 5.0 ns MD simulations, we did not use snapshots of the first 500 ps for analyses as equilibration stages. Using snapshots of the remaining 4.5 ns, we calculated distribution density profiles for the internal water molecules and H-bond patterns inside the cavity. Water molecules inside the cavity were identified using the triangulation procedure proposed by Bakowies and van Gunsteren.⁶² We judged that a water molecule was located inside the cavity at time *t* when a water molecule remained inside a polyhedron formed by the Ca

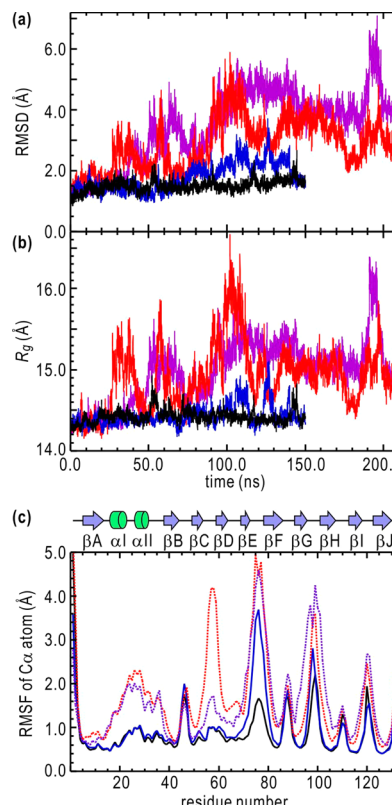


Figure 2. (a) Time course of RMSD values for the protein backbone atoms (black, STE_NPT_run1; blue, STE_NPT_run2; red, apo_NPT_run1; purple, apo_NPT_run2). (b) Time course of R_g values for each run. The colors used are the same as in panel a. (c) RMSF values of the $C\alpha$ atoms of the protein. The colors used are the same as in panel a. Straight and broken lines represent the STE-bound and apo forms, respectively. The values were calculated using the snapshots captured between 0 and 150 ns and between 60 and 210 ns in the runs for the STE-bound and apo forms, respectively. The secondary structures illustrated above are taken from the HELIX and SHEET records in the PDB file of 1HMT.¹³

atoms of the protein and the supplementary points listed in Table S1 (Supporting Information) between *t* and *t* + Δt . We chose 5 ps (100 snapshots) as the time window Δt .

Next, we calculated the distribution densities of the internal water molecules.^{63,64} The boxes were partitioned into 0.5 Å × 0.5 Å × 0.5 Å voxels, and a water oxygen or a water hydrogen atom in each snapshot was assigned to a voxel where the atom was detected. The distribution density of water was calculated using the equation

$$\rho(\vec{r}_k) = q_{\text{total}}(\vec{r}_k)/N_{\text{snapshot}} \quad (1)$$

where $q_{\text{total}}(\vec{r}_k)$ is the sum of the atomic number of atoms visiting the *k*th voxel \vec{r}_k , and N_{snapshot} is the total number of snapshots used for the calculation.

To examine time-averaged H-bond patterns, we calculated “cube–cube H-bond” (ccHB) patterns, as proposed by Yokomizo et al.^{65,66} Briefly, when two non-hydrogen atoms form an H-bond, the pair of voxels containing the two atoms is regarded as being in a ccHB. The ccHB patterns were examined in every snapshot, and then we calculated the ccHB formation probability between two voxels \vec{r}_i and \vec{r}_j using the equation

$$P_{\text{ccHB}}(\vec{r}_i, \vec{r}_j) = N_{\text{ccHB}}(\vec{r}_i, \vec{r}_j)/((N_{\text{detect}}(\vec{r}_i) + N_{\text{detect}}(\vec{r}_j))/2) \quad (2)$$

Table 1. Summary of Each NVT MD Simulation for Calculation of the Water Distribution Map and the ccHB Patterns

run name	snapshot used for initial coordinates	RMSD value and SD of the protein main-chain atoms ^a	RMSD value and SD of STE atoms ^a	average number and SD of internal water molecules ^b
run for STE_closed_form	116.0 ns in STE_NPT_run1	1.61 ± 0.12	1.77 ± 0.32	26.06 ± 2.74
run for apo_closed_form	20.0 ns in apo_NPT_run1	1.84 ± 0.20		35.84 ± 3.44
run for fully_open_form	194.0 ns in apo_NPT_run1	3.61 ± 0.30		63.92 ± 7.33

^aThe time courses of the RMSD values are shown in panels a–c of Figure S3 in Supporting Information. ^bThe time courses of the numbers of the internal water molecules are shown in panels d–f of Figure S3 in Supporting Information.

where $N_{\text{ccHB}}(\vec{r}_i, \vec{r}_j)$ is the number of snapshots in which ccHBs are formed between voxels \vec{r}_i and \vec{r}_j , and $N_{\text{detect}}(\vec{r}_i)$ is the number of snapshots in which a non-hydrogen atom visits a voxel \vec{r}_i . We used the criteria proposed by Yokomizo et al. to determine H-bonding.^{65,66} For calculation of ccHB patterns, the voxel size was set to 1.5 Å × 1.5 Å × 1.5 Å.

2.3. MD Simulation of Pure Water. To compare the hydration structure inside the FABP3 binding cavity to that in bulk water, we performed an MD simulation for pure water, using MARBLE. The initial dimensions of the box were 30.00 Å × 30.00 Å × 30.00 Å, and the system was placed under periodic boundary conditions. The box contained 856 TIP3P water molecules and no ions. Water molecules were treated as rigid bodies and we used a time step of 2 fs. After an energy minimization of 1000 steps, the system was heated to 310.15 K over a period of 100 ps and subsequently equilibrated over 900 ps under an NPT condition at 1 atm. Then the system was switched to an NVT condition and a 3 ns MD simulation was performed. The first 500 ps of the NVT run were discarded as the equilibration period. For the last 2.5 ns, the structure was saved every 50 fs. Using these snapshots, the average distribution density and the ccHB formation probability were calculated as described in the previous section.

3. RESULTS

3.1. MD Trajectory of FABP3 in the STE-Bound Form.

We first performed two 150 ns MD simulations for the STE-bound form of FABP3 (STE_NPT_run1 and STE_NPT_run2) at 310 K. In these simulations, the average root-mean-squared deviation (RMSD) values of protein main-chain atoms from the energy-minimized structure were 1.50 ± 0.29 Å (STE_NPT_run1) and 1.76 ± 0.45 Å (STE_NPT_run2) (Figure 2a). The RMSD values over 2.0 Å can be explained by the positional deviations of the N- and C-terminal ends from the energy-minimized structure, and by the opening of the portal. To monitor the degree of opening, we calculated the radius of gyration R_g of the protein in each snapshot, using the following equations:

$$R_g^2 = \sum_{i=1}^N m_i r_i^2 / \sum_{i=1}^N m_i$$

$$r_i^2 = |\vec{r}_i - \vec{r}_{\text{COM}}|^2 \quad (3)$$

where N is the number of protein atoms, m_i and \vec{r}_i are the atomic weight and position vector of the i th protein atom, respectively, and \vec{r}_{COM} is the position vector of the center of mass of the protein molecule. In the STE-bound form, the R_g values fluctuated around 14.4 Å throughout the simulations (Figure 2b). Because the R_g value of the crystal structure was 14.1 Å, it follows that the protein fluctuated around the crystal structure in a closed conformation.

Next, we calculated the root mean-squared fluctuations (RMSFs) of protein $C\alpha$ atoms using all snapshots captured from 0–150 ns (Figure 2c). The calculated RMSF values were less than 1.0 Å for almost all protein residues, indicating that this protein is rigid in the STE-bound form. The α -helical region and the β D and β E strands displayed the RMSF values of approximately 0.8 Å, slightly higher than the other β -strand regions (<0.6 Å); the relatively large positional fluctuation in these regions was also observed in the structure solved by the solution NMR.¹⁶ The smaller RMSF values observed in the C–D loop compared with those in the other loops were due to interactions with bound STE, α II, and the loop connecting α II and β B. The distances between carbon atoms of the bound STE and the atoms on α II remained nearly constant during the simulations, indicating that the hydrophobic interactions between the protein and STE keep the portal in a closed conformation (Figure S2 in Supporting Information).

The protein showed a closed conformation in most snapshots as illustrated in Figure 3a, and it rarely displayed an open conformation with $R_g > 14.6$ Å. When the protein showed the open conformation, the β E strand and the E–F loop move outward, and the gap and the portal open (Figure

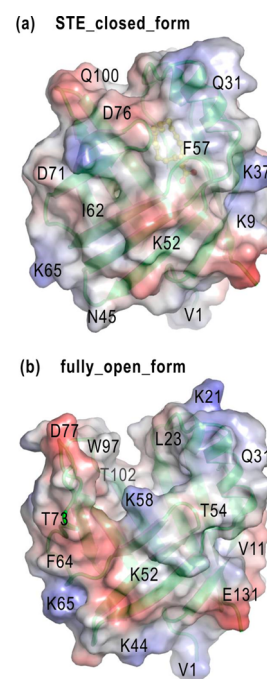


Figure 3. Surface representations of the protein structures observed in the simulations. (a) The protein structure in the 116 ns snapshot of STE_NPT_run1. The portal was closed and this structure is referred to as “STE_closed_form”. (b) The protein structure in the 194 ns snapshot of apo_NPT_run1. Both the portal and the gap were open and this structure is referred to as “fully_open_form”.

4). In this conformation, the E–F loop is not in contact with the bound STE or α II, resulting in the large RMSF values

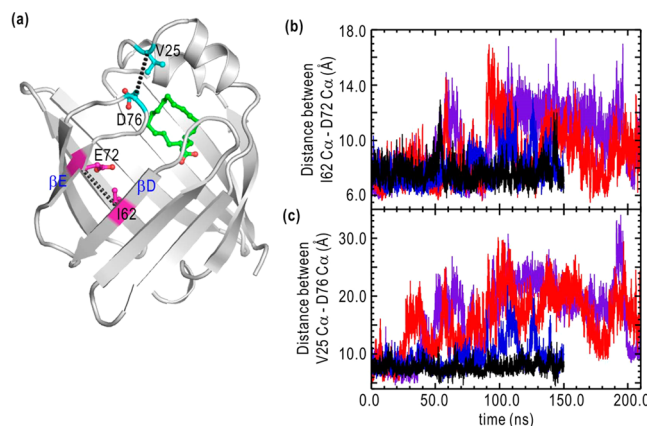


Figure 4. (a) Positions of I62, E72, V25, and D76 in the crystal structure of FABP3. (b,c) Time course of the distances between the C α atoms of I62 and D72, and between the C α atoms of V25 and D76, respectively. The black, blue, red, and purple lines represent the distances in the STE_NPT_run1, STE_NPT_run2, apo_NPT_run1, and apo_NPT_run2 simulations, respectively.

observed for this region in STE_NPT_run2. However, this conformation is transient in the STE-bound form, and the protein soon recovers the closed conformation, due to hydrophobic interactions with the bound STE (Figure S2 in Supporting Information).

3.2. MD Trajectory of FABP3 in the Apo Form. FABP3 in the apo form at 310 K was in an open form in most snapshots. The average RMSD values for the protein main chain were 2.86 ± 0.83 Å (apo_NPT_run1) and 3.49 ± 1.19 Å (apo_NPT_run2), and the average R_g values were 14.9 ± 0.39 Å (apo_NPT_run1) and 15.0 ± 0.38 Å (apo_NPT_run2) (Figure 2). The widths of the gap and the portal were significantly larger than in the closed form (Figure 4), and in the apo protein, the opened portal functions as a channel connecting the cavity with the bulk (Figure 3b). The diameter of the channel was approximately 11–14 Å in the 194.0 ns snapshot in apo_NPT_run1, for example, and thus water molecules are expected to behave as bulk solvent near the center of the fully open channel.

The RMSF values calculated using the snapshots captured between 60 and 210 ns were much larger than those for the STE-bound form (Figure 2c). The α -helical domain and the loops facing the α -helical domain (the C–D, E–F, and G–H loops) showed particularly large fluctuations, which were consistent with the results obtained from solution NMR of iLBPs.^{67–69} The fluctuations of the C–D loop were much larger in apo_NPT_run1 than in apo_NPT_run2, indicating that the loop displayed different dynamics in the two simulations. This result suggests the possibility that the protein has at least two different modes for the opening motion, while the gap and the portal open wide in both modes.

3.3. Distribution of Water Molecules inside the Cavity. In the FABP3 crystal structures, 13 water molecules are present inside the binding cavity, and they interact with each other through H-bonds. To investigate the properties of the water cluster, we performed additional 4.5 ns NVT MD simulations using the snapshots captured in the NPT simulations as the initial structures. By using trajectories in which the protein and

the bound STE do not undergo any significant conformational changes (Figure S3 in Supporting Information), we can characterize hydration structures under steady-state conditions. We obtained such trajectories in runs performed for the three forms: STE_closed_form, apo_closed_form, and fully_open_form (Table 1). For these runs, we calculated the water distribution densities and the time-averaged H-bond patterns inside the cavity, with only the internal water molecules identified with the aid of the triangulation method.⁶²

To obtain the cavity hydration structure for the open conformation of the ligand-bound state, we also performed NVT simulations for the STE-bound protein, starting from the open form. However, even in only 3.0 ns simulations, the protein preferentially showed the closed conformation and did not maintain the open conformation (Figure S4 in Supporting Information). Therefore, we were unable to use these trajectories for characterization of the internal water molecules in the STE-bound open form.

Figure 5 shows the distribution densities of the internal water molecules. In STE_closed_form (Figure 5a), the water cluster

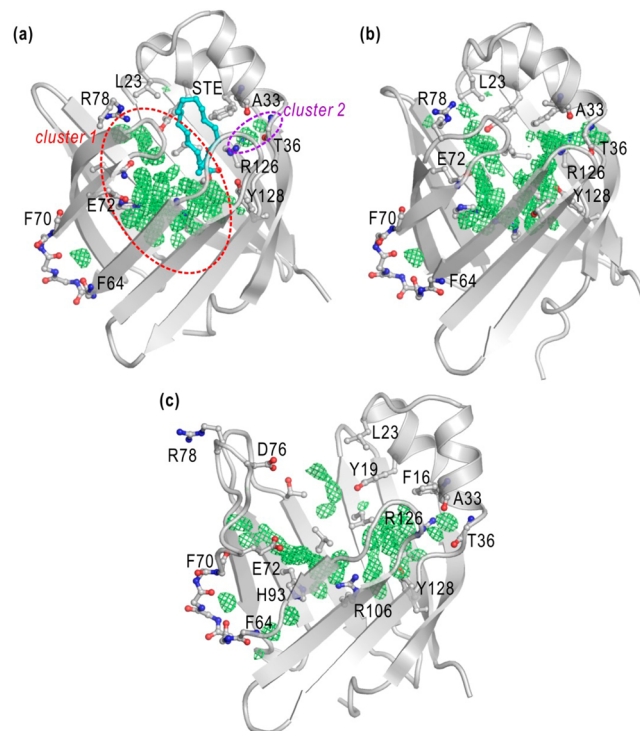


Figure 5. Distribution density maps of the water molecules located in the binding cavity are shown in green mesh. The contour level of the maps is 0.0625 e/(0.5 Å) 3 . (a) The map for STE_closed_form. (b) The map for apo_closed_form. (c) The map for fully_open_form. The protein structure captured in the last snapshot of each simulation is shown by the gray cartoon model, and STE is shown by the cyan stick model. The side chains of residues F64–F70 and all hydrogen atoms are not shown.

was highly structured. The density peak values were more than 2-fold higher than the average water density calculated in the pure water simulation (0.044 e/(0.5 Å) 3). Two water clusters were present and they were separated by the bound STE. The larger cluster (cluster 1) was located on one side of the STE and connected to the bulk solvent through the gap. The smaller cluster (cluster 2) was composed of two water molecules and interacted with the guanidium group of R126 and the protein

main-chain atoms on the loop connecting α II and β B. When compared with the electron density map, the calculated water density distribution was deviated from the map due to the structural deviations from the crystal structure in the simulation, but peak shapes of the calculated water density distribution were still near spherical, and the peak positions were located within the H-bond distances from each other. This indicates that water molecules at the hydration sites were highly ordered and structured (Figure S5 in Supporting Information).

The water density distribution in apo_closed_form was similar to that in STE_closed_form, except that clusters 1 and 2 were merged into a single cluster (Figure 5b). Around polar protein atoms lining the cavity, water molecules were distributed similarly to those in STE_closed_form. However, the density near the center of the cavity, which was occupied by the STE alkyl chain in STE_closed_form, was lower than around the polar protein atoms. This region was partially in contact with the hydrophobic surface of α II, and thus the water structure in this region was disordered. The disorder of the internal water molecules could trigger the shift from the closed form to the open form. Consequently, in fully_open_form, the cavity is connected to the bulk solvent through the open portal, and the hydration sites displaying high distribution densities are limited to near the polar protein atoms (Figure 5c).

3.4. ccHB Pattern. In the previous section, we showed that the hydration density profiles in the binding cavity differed among the three forms. This result indicates the possibility that the water dynamics and H-bond profiles also differ among the three forms. Because the H-bond networks in and around protein molecules are essential for protein dynamics and structural stabilization,^{24–28} it may be helpful to characterize the H-bond networks in the binding cavity to illuminate the effect of the internal water cluster on the protein conformation. Therefore, we calculated ccHB patterns using the 4.5 ns NVT trajectories to examine the time-averaged H-bond patterns in the binding cavity.^{65,66}

In STE_closed_form (Figure 6a), the calculated ccHB pattern displayed coherent ordering in the vicinity of the polar protein atoms and the STE carboxyl group. The R126 side chain not only interacted with the STE carboxyl group, but also fixed the loop connecting α II and β B at A33 and T36 via the two resident water molecules in cluster 2. Remarkable bundles of ccHBs were formed between the STE carboxyl group and the R106 side chain, indicating that this side chain, in addition to the R126 and Y128 side chains, is important for holding a FA carboxyl group inside the cavity, via one or two water molecules. Another bundle of ccHBs was emitted from the R106 side chain toward the E–F loop (T73–R78), and this H-bond was a part of the H-bond network reaching the E72 side chain. Near the gap region (Figure 7a), coherent patterns of ccHBs were also formed between L51/T53/T60 and E72/T73. The β -strands were interconnected by three or four H-bonds formed between these well-conserved residues (Figure S1 in Supporting Information).²³ On the other hand, near the alkyl chain of STE, the ccHB patterns were less ordered. The alkyl chain showed RMSF values of around 1.4 Å, higher than those in the C–D and E–F loops (around 0.8–1.0 Å) (Figure S6 in Supporting Information), indicating the fatty acid showed a certain degree of positional fluctuation even in the closed binding cavity. Because water molecules are able to form H-bonds with adjacent water molecules even when located near the hydrophobic chain, these results suggest the possibility that the H-bond network is rearranged in synchrony with the

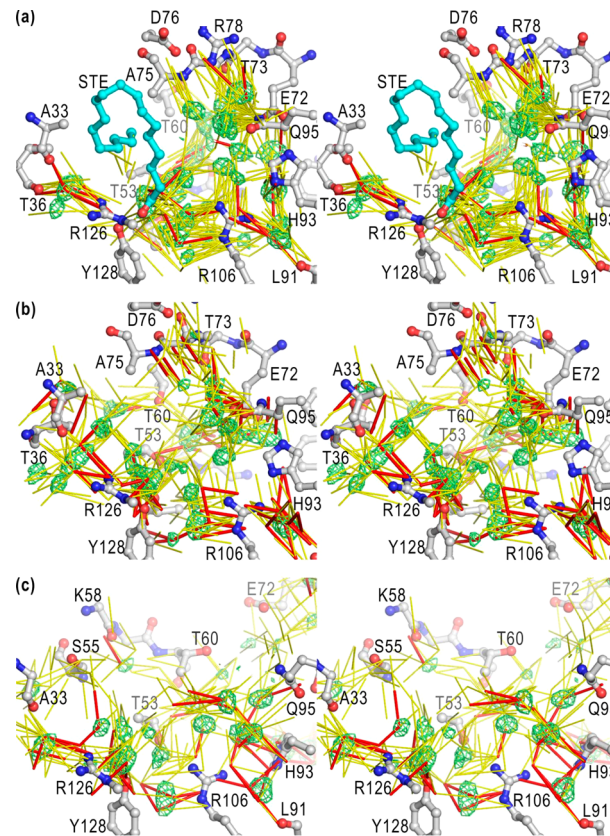


Figure 6. ccHB patterns in the binding cavity. Thin yellow sticks indicate ccHBs with $P_{\text{ccHB}} \geq 0.135$ (2.1 times larger than the average value of the bulk solvent, 0.0652) and $P_{\text{ccHB}} < 0.270$ (4.1 times larger than the average value of the bulk solvent). Thick red sticks indicate ccHBs with $P_{\text{ccHB}} \geq 0.270$. The protein and STE structures captured in the last snapshot of each NVT simulation are indicated by the stick-ball model. Red and blue atoms show oxygen and nitrogen atoms, respectively. Gray and cyan atoms show carbon atoms of the protein and STE, respectively. The green mesh represents hydration water sites with a density $> 0.100e/(0.5 \text{ \AA})^3$. Panels a, b, and c show the ccHB patterns in STE_closed_form, apo_closed_form, and fully_open_form, respectively.

motion of the flexible alkyl chain as illustrated in Figure S7 in Supporting Information.

In apo_closed_form (Figure 6b), R126 and the loop connecting α II and β B interacted via water molecules as in STE_closed_form. The H-bonds emitted from the R106 side chain toward the Y128 side chain were conserved, even in the absence of the bound FA. However, in the apo form, the H-bonds emitted from the same side chain toward the E–F loop were largely disturbed. The H-bond network around the gap was formed between L51/T53/T60 and E72/T73, but the ccHB patterns fluctuated greatly (Figure 7b). At the positions occupied by the STE alkyl chain in STE_closed_form, the H-bond patterns were disordered, as deduced from the low water distribution density.⁶⁵ The disorder of the internal water in apo_closed_form could drive the protein to the open conformation to gain water entropy. In fully_open_form, the internal water displays a completely disordered ccHB pattern in the region that is not in contact with the inner protein surface (Figure 6c). This ccHB pattern resembles the pattern observed around the outer surface of a soluble protein,⁶⁵ implying that the cavity environment in fully_open_form is similar to the environment around protein outer surfaces. Around the gap,

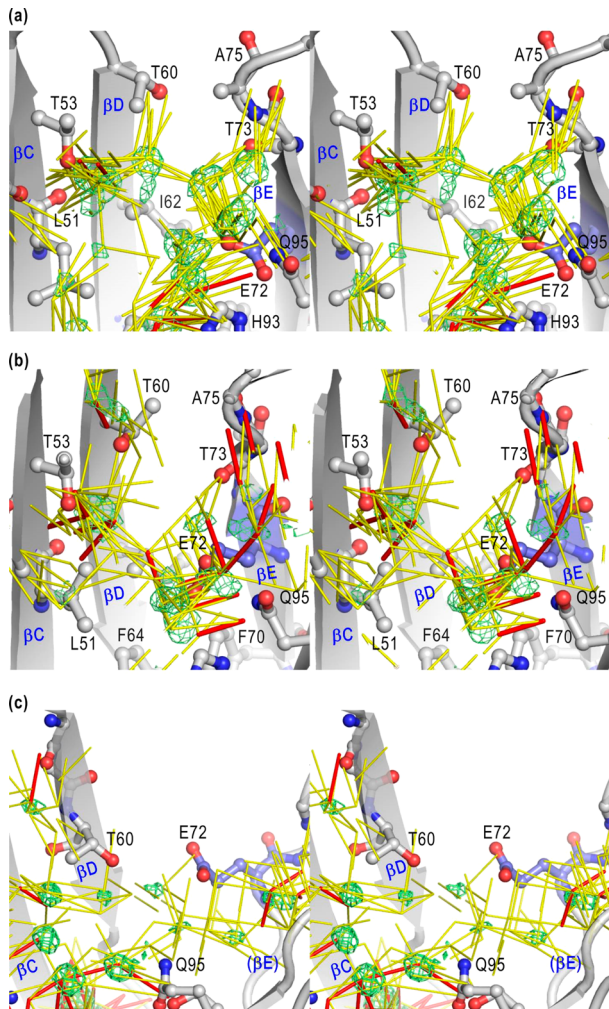


Figure 7. ccHB patterns around the gap. The details of the representation are identical to Figure 6. The E72 residue is highlighted in blue. Panels a, b, and c show the ccHB patterns of STE_closed_form, the apo_closed_form, and the fully_open_form, respectively.

stable H-bond patterns were no longer observed, and the residues E72 and T60 were rarely connected by H-bonds (Figure 7c).

To examine the differences in the H-bond properties in the binding cavity among the three forms, we computed the distributions of P_{ccHB} (Figure 8). The numbers of ccHBs showing $P_{\text{ccHB}} < 0.100$ are largest in fully_open_form and secondarily in apo_closed_form (Figure 8a). This stems from the total number of ccHBs and the cavity volume. The total number (88280) was largest in the fully_open_form, indicating that the volume accessible to water molecules is largest in this form. Conversely, in STE_closed_form, the bound STE limits the space accessible to the internal water molecules, and the total number of ccHBs is only 23788. Thus, the number of ccHBs showing $P_{\text{ccHB}} < 0.100$ was smallest in STE_closed_form. On the other hand, the number of ccHBs showing $P_{\text{ccHB}} > 0.110$ was nearly identical among the three forms, despite the large differences in the total numbers of ccHBs (Figure 8b). This result implies that the H-bond patterns are disordered in most parts of the binding cavity in apo forms. The disorder of the water is especially significant in the fully_open_form, since the cavity is connected with the bulk solvent through the open portal.

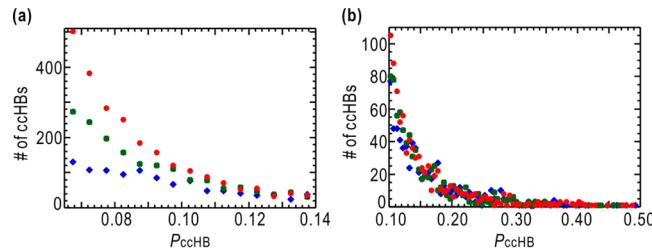


Figure 8. P_{ccHB} distributions in each NVT simulation. The ranges for P_{ccHB} shown are 0.065–0.14 in panel a and 0.1–0.5 in panel b. Blue diamonds, green squares, and red circles represent the numbers of binned ccHB pairs in STE_closed_form, apo_closed_form, and fully_open_form, respectively. The widths of the bins for the P_{ccHB} distributions were set to 0.005. The total numbers of ccHB pairs were 23 788, 46 059, and 88 280 in STE_closed_form, apo_closed_form, and fully_open_form, respectively.

3.5. Interaction Dynamics between Water Molecules and Polar Protein Atoms Facing the Cavity. From the ccHB and hydration density analyses, we obtained the average hydration structures in the binding cavity, and three-dimensionally illustrated that the hydration structures differ between the apo and STE-bound forms. Based on these results, we suppose that the internal water molecules are more mobile in apo forms because of the larger space available. However, the calculated hydration structures are time-averages from short 4.5 ns simulations only; this short simulation time was required to keep the protein and STE conformations relatively unchanged, in order to calculate static hydration structures. To obtain a statistically reliable support for the results presented in the previous sections, we needed to characterize the water dynamics inside the cavity using much longer snapshots.

In addition, because we are now interested in the effects of internal water molecules on the protein conformation, we here focused on the water dynamics around polar protein atoms facing the cavity. To describe the dynamics unique to internal water molecules, we calculated two quantities for each polar atom:

$$\text{Ratio_Contact} = \frac{\text{NContact}}{N_{\text{snapshot}}} \times 100\% \quad (4)$$

$$\text{Ratio_NWater} = \frac{\text{NWater}}{N_{\text{total water}}} \times 100\% \quad (5)$$

NContact is the number of snapshots in which a polar protein atom H-bonded with a water molecule, and N_{snapshot} is the total number of snapshots used. NWater is the number of water molecules with which a polar protein atom H-bonded in the snapshots used, and $N_{\text{total water}}$ is the total number of water molecules. For this calculation, each water molecule was tagged and individuated. In this context, when a water molecule revisits a hydration site of a polar protein atom after it leaves the same site, NWater is not incremented and NContact is incremented by one. The use of tagged water molecules was necessary to avoid multiple counting of identical water molecules in NWater, because it is probable that an H-bond between two particular atoms could be temporarily broken by positional fluctuations, although an H-bond is formed between the two atoms in a large number of snapshots.

Because most polar atoms face the bulk solvent, the Ratio_NWater value was roughly proportional to the Ratio_Contact value (Figure S8a in Supporting Information). This is

Table 2. Comparison of Ratio_Contact and Ratio_NWater Values for the Atoms Lining the Cavity in the STE-Bound and Apo Open Forms

atom	STE_NPT_run1 (0–150 ns)			apo_NPT_run1 (60–210 ns)		
	ASA (Å ²)	Ratio>Contact (%) ^a	Ratio_NWater (%) ^b	ASA (Å ²)	Ratio>Contact (%) ^a	Ratio_NWater (%) ^c
T53 OG1	11.06	95.71	11.36	10.95	90.06	47.35
T60 OG1	18.70	97.29	75.30	18.07	94.24	82.57
E72 OE1	12.15	81.25	16.76	20.76	99.05	76.75
E72 OE2	7.60	75.00	15.45	21.46	99.69	76.29
T73 O	11.73	93.11	44.77	23.20	91.04	94.45
A75 N	3.82	86.12	8.87	24.99	78.16	62.44
R78 NH2	4.49	91.76	8.38	30.02	87.78	91.02
L91 O	0.53	76.36	0.20	0.36	78.12	0.06
H93 ND1	1.27	83.85	7.43	1.43	91.07	22.33
Q95 OE1	9.42	95.02	10.11	13.44	84.91	61.31
R106 NE	3.78	96.96	3.64	2.11	97.38	6.61
R106 NH1	5.02	98.48	5.84	3.54	99.74	15.08
R106 NH2	14.42	98.68	9.44	16.84	98.56	40.68
R126 NE	0.00	0.12	0.15	2.59	92.61	13.04
R126 NH1	3.09	89.54	12.47	6.43	86.69	31.39
R126 NH2	1.18	98.24	3.11	10.26	99.24	38.36
Y128 OH	0.63	29.45	4.73	12.43	94.80	26.94

^aThe number of snapshots used for the calculations (N_{snapshot}) was 150 000. ^bThe total number of water molecules in the simulation box ($N_{\text{total water}}$) was 9962. ^cThe total number of water molecules in the simulation box ($N_{\text{total water}}$) was 9980.

consistent with the fact that hydration sites on protein outer surfaces are visited by many water molecules but their resident time at the site is generally very short.^{70–72} In contrast, water molecules located in protein cavities are generally long-lived^{70–72} because of low water mobility.⁷³ This indicates that polar protein atoms lining the inner cavity could interact with only a limited number of water molecules during a simulation, and it follows that the Ratio_NWater values were generally low with high Ratio>Contact values.

When calculating the ratios from 150 ns long trajectories in STE_NPT_run1, the Ratio_NWater values were less than 20%, whereas the Ratio>Contact values were more than 70% for the most polar protein atoms lining the binding cavity (Figure S8b in Supporting Information). This indicates that the water molecules inside the cavity have low mobility. In contrast, in the apo open form, the Ratio_NWater values were much larger for most atoms, despite the comparable values for Ratio_NContact (Table 2). For the atoms on the E–F loop (the polar atoms of E72, T73, A75, and R78), the increase in the Ratio_NWater values can be explained in terms of significant increases in the ASA values. Ratio_NWater values of the atoms interacting with the carboxyl group of STE in STE-bound form (R126 NE and Y128 OH) are also increased because the atoms are solvent-exposed in the apo form. For the other atoms shown in Table 2, the ASA and Ratio_NContact values were comparable with those in STE_NPT_run1, and thus the increase in the Ratio_NWater values implies that the exchange of the hydration water molecules at the hydration sites around the polar protein atoms more often occur in the binding cavity in the apo open form. This can be explained by the higher mobility of the internal water molecules because of the larger volume accessible to the water molecules and because of the fully open portal.

Next we tried to compare the ratios in the closed conformations, but the time periods when the protein was in closed form were only first 25 ns in the two NPT runs of apo FABP3. Thus, we computed the ratios using only the first 25 ns of the trajectories to get the preliminary results for the closed

forms (Tables S2 and S3 in the Supporting Information). In this case, the Ratio_NWater values were very small compared to the values shown in Table 2, because the local minima the system could visit were limited due to the shorter time period used for the calculation. Therefore, the comparison of the values from the trajectories of the short time period is statistically unreliable. However, the Ratio_NWater values calculated from the two runs of the apo form were nearly more than twice those for the STE-bound form calculated from the first 25 ns of the trajectories (Tables S2 and S3 in Supporting Information). From this result, we suppose that in the apo forms, the internal water molecules have a tendency to have higher mobility than those in the STE-bound form, and consequently the H-bond patterns in the cavity could be disturbed as shown in Figures 6 and 7.

4. DISCUSSION

Through the MD simulations of apo FABP3 at 310 K, we presented the possibility that, in addition to the α -helices, the β D/ β E gap is also involved in channel opening for FA entry. Then we demonstrated that the hydration structures in the binding cavity differ drastically between the STE-bound and apo forms. This suggests that the internal water structure is controlled by the presence and absence of the bound LCFA and plays a key role of the opening of the portal and the gap together with bound LCFAs. Based on the results of the MD simulations and the hydration structure analyses inside the cavity, we discuss why open conformation is predominant in the FABP3 apo form and then the relevance of the internal water molecules to FABP3 biological roles in living cells.

4.1. Comparison of the Structures for the Apo Form of FABP3 Determined in Our Simulation and in Experimental Studies. In our simulations, apo FABP3 mainly showed an open conformation (Figure 2) and the portal functioned as a channel connecting the cavity to the bulk solvent (Figure 3). The diameter of the channel was approximately 11–14 Å in a snapshot, sufficiently wide to allow bulky molecules, such as ANS or carbazole derivatives, to

pass through.^{7,15,31–33} However, crystal structures of the apo state deposited in PDB are very similar to those of FA-binding forms,^{34,35} inconsistent with the open conformation observed in our simulations.

These differences would be due to the crystal packing. In the FABP3 crystal in the space group $P2_12_12_1$, the α II helix and the β D strand contacts with the symmetry-related molecules (Figure S9 in Supporting Information). Therefore, the tight packing of the α -helical region may suppress the domain motion of this region and thus the protein may show the closed conformation in the crystal. When we performed a simulation of FABP3 in apo form in crystalline environment, the proteins primarily showed the closed conformation illustrated by the RMSD values of around 1.5–2.0 Å and the R_g values of around 14.5 Å (Figure 9). The small standard deviations of the R_g

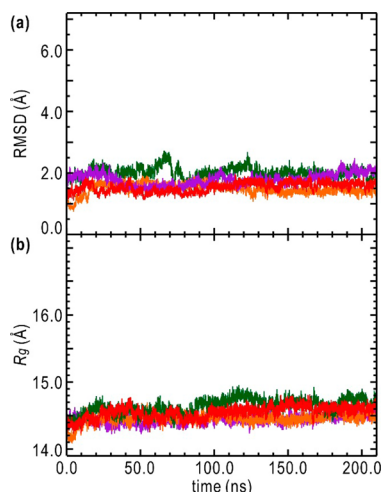


Figure 9. Time courses of RMSD of the protein backbone atoms from their initial structures (a) and protein R_g values (b) of apo FABP3 in the crystalline environment. Red, orange, green, and purple lines indicated the values of molecules 1, 2, 3, and 4 in the unit cell, respectively. The average values and standard deviations of the R_g were 14.5 ± 0.09 , 14.4 ± 0.07 , 14.6 ± 0.11 , and 14.5 ± 0.08 Å, respectively. The details of the simulation are described in the Supporting Information.

(0.07–0.11 Å) indicates the large motion observed in the simulations in the solution environment is suppressed in the crystalline environment. This simulation result also implies that the apo open structure observed in our MD simulations is not completely artificial, but is the presumable structure in solution environments. The small deviation of the simulated structures from the crystal structure, indicated by the RMSD values over 2.0 Å and R_g values over 14.6 Å, might be explained in terms of the temperature of the crystals at the diffraction data collection.⁷⁴ Now most protein structure models are solved at ~ 100 K to minimize radiation damage of protein crystals, and the crystals are flash-cooled before data collection.⁷⁵ However, it is also considered through the systematic analyses that the protein molecules shift to low-enthalpy states during the flash cooling and the cryo-structures are not always identical to those at ambient temperatures, which could be relevant for their biological functions.^{76,77} For the case of FABP3, the protein might favorably show the closed conformation in crystal at cryogenic temperatures, which could be the low-enthalpy form of the protein but seems to be unsuitable for the ligand loading.

In our simulations performed in the solution structure, the full opening of the channel is accomplished by movement of the β D- β H strands and the α -helical region. A hydrogen/deuterium exchange analysis of apo chicken liver bile acid-binding protein (cL-BABP) at 25 °C showed that the protection factors of the β D- β H strands of the protein are comparable to those of α II. This indicates that the β D- β H strands display opening fluctuations that are as large as those displayed by the α -helical region.⁷⁸ Because the sequential identity between FABP3 and cL-BABP is 33% and their ligand binding modes are largely different, insights obtained using cL-BABP may not be directly applicable to FABP3. However, the fact that these two proteins had similar 3D structures and showed similar dynamic behaviors implies that the global dynamics at the α -helical region and the edge of the β -strands observed in this study are common, inherent features of iLBPs.

4.2. Role of Amino Acid Residues Lining the Binding Cavity.

In STE_closed_form, we observed a coherent H-bond pattern in the binding cavity (Figure 6a), and the H-bond network interconnected multiple β -strands. The H-bond network was anchored by the polar atoms of the residues T53, T60, E72, T73, and R106. These residues are highly conserved in FABP subfamily IV (Figure S1 in Supporting Information),²³ implying that they play indispensable roles in facilitating H-bond network formation and possibly in stabilizing the protein structure.

In general, water molecules around polar protein atoms are positioned within a limited distance and angle range viewing from the polar protein atoms.⁶¹ It follows that hydration sites around polar protein atoms are essentially defined only by tertiary or quaternary structures.⁵⁹ In our simulations, the water distribution around polar protein atoms lining the cavity was similar between STE_closed_form and apo_closed_form (Figure 5). However, in apo_closed_form, water molecules were able to move more freely within the inner cavity, resulting in a less ordered H-bond pattern. Binding of FA narrows the space accessible to water molecules, and water molecules lose their mobility and tend to reside at the defined hydration sites. Consequently, in the STE-bound form, an extensive and stable H-bond network is formed in the binding cavity between the polar protein atoms lining the cavity and the bound FA (Figures 1, 6, and 7). To construct this stable H-bond network within the rigid β -barrel, the hydrophilic residues lining the cavity each serve an important function and their polar atom positions are finely tuned.

A mutational study has been published that supports this hypothesis; e.g., in the E72S mutant, the binding affinity is almost same as that of the wild type, but the protein loses significant stability.⁷⁹ Because E72 is located in the gap region (Figure 7), this residue may play an important role in protein stabilization.

4.3. The Relationship among the Protein, Bound FA, and Internal Water Molecules. The closed conformation is mainly realized and stabilized through hydrophobic interactions between a hydrophobic ligand and hydrophobic protein residues. In FABP3, as well as in other iLBP members, the hydrophobic residues are located in the portal region, and they show a certain degree of positional fluctuation, even when FA is bound (Figure 2c). A large part of the bound FA (C6 to C18) is in contact with the flexible regions of the protein (Figures S2 and S6a in Supporting Information), and thus thermal motion of FA is permitted in the closed binding cavity (Figure S6b in Supporting Information). The internal water molecules are

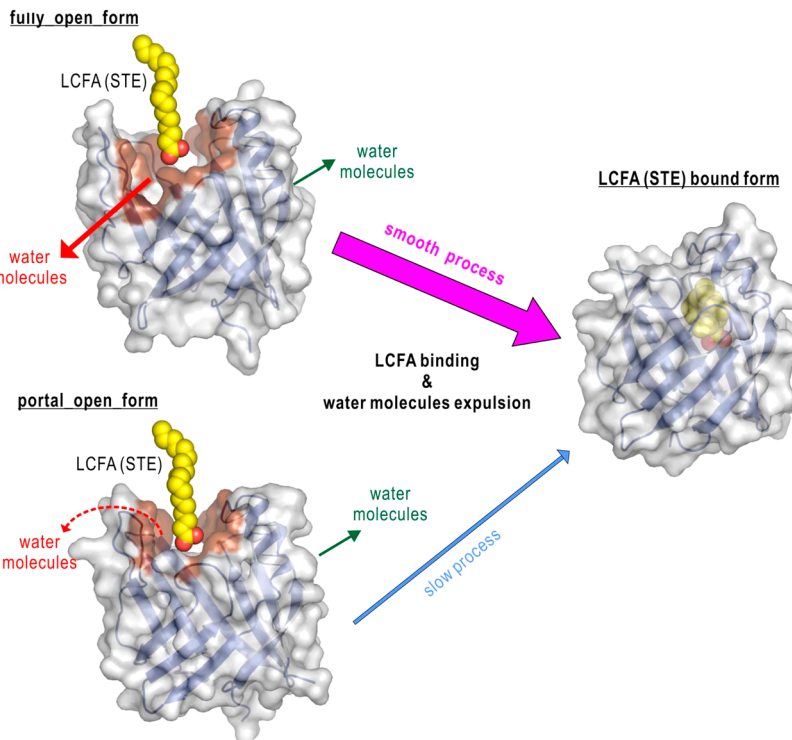


Figure 10. Diagrammatic illustration of the hypothetical mechanism for LCFA binding to the FABP3 internal binding site. The entrance to the internal cavity is highlighted in brown. When the portal and the gap are both open (fully_open_form), FABP3 has two putative water-exchange pathways: the gap (red arrow), and the back side portal (green arrow). Exchange between LCFA and the internal water molecules would occur efficiently in this form, and LCFA binding would progress smoothly. If the gap is closed and only the portal is open (portal_open_form), the water exchange-pathway is limited to the back side portal (green arrow), and the efficiency of the replacement of the internal water molecules by LCFA is expected to be less than half of that in fully_open_form. Therefore, in this form, the LCFA binding would be slower than that in fully_open_form.

surrounded by the protein and the bound FA, and their motions are inevitably subject to the motions of the protein and the bound FA. Consequently, the water molecules are not fixed in single positions, but move in synchrony with FA as illustrated in Figure S7 in Supporting Information. Therefore, we can say that the H-bond network is sufficiently robust to tolerate the thermal motion of bound FA. The binding cavity permits the FA and the internal water molecules to coexist, increasing the stability of the protein.

4.4. Opening Mechanism in Apo FABP3. The conformational shift from the open to closed conformation is triggered by binding FA or another hydrophobic molecule, and in the apo form, the protein predominantly shows the open conformation, permitting the ligand to easily enter the binding site. The gap between the β D- β E strands is indispensable for the open conformation. The two strands are not within H-bond distance, and are only connected by two or three water molecules interacting with T53/T60 on β D and E72 on β E, respectively (Figure 7). When a FA molecule binds, the internal water molecules are ordered, and a stable H-bond is formed in the binding cavity. The water molecules connecting the β D/ β E strands are part of an extensive H-bond network. As a result, the gap is closed and the two water molecules function as a “latch” for closing the gap. In the E72S mutant, the H-bond network around this residue may be disturbed and the water-mediated interaction between the β D and β E strands may be weakened; consequently, in the mutant protein, the gap may not stay closed.

On the other hand, in the apo form, H-bond patterns were disordered even in the closed form (Figures 6 and 7). Thus,

dissociation of H-bonds around the gap frequently occurs and the interaction between β D and β E is clearly much weaker than the interstrand interactions that form β -sheets. Consequently, the gap opens, accompanied by portal opening, and the protein shifts to the fully_open_form (Figure 4), in which water molecules gain much larger entropy than they possess in the closed cavity.

4.5. Biological Relevance of the Internal Water Molecules to FABP3. The present MD simulations elucidated a novel fully open structure of FABP3 that is achieved by the opening of both the portal and the gap. Given the molecular mechanism of FA-FABP3 binding, the fully open FABP3 conformation is an important structure for FA loading. With respect to FA loading into FABP3, this wide-open protein conformation should facilitate substitutions between FA ligands and internal water molecules in the large binding cavity. The binding cavity in the apo form is filled by approximately 60 water molecules (Table 1). When an LCFA molecule enters the binding site, the internal water molecules must be expelled from the cavity. In the “half-open” form of FABP3, in which the portal is open but the gap is closed, which was observed in the snapshot captured at 120.0 ns in apo_NPT_run1 (portal_open_form in Figure 10), the diameter of the channel was 7–10 Å, sufficient for entry of a single LCFA molecule. However, for the exit of the internal water molecules accompanying LCFA loading, the internal water molecules require an exit other than the portal. An MD simulation study of rat FABP2 indicated that internal water molecules exchange with the bulk solvent through the “back side portal” (portal PII),⁴⁹ which corresponds to the row of water molecules referred to as cluster

2 in the present study (Figure 5). The Ratio_NWater values of R126 NH1/NH2 showed far more active water exchange at cluster 2 in the apo form (30%–40%) than in STE-bound form (<13%) (Table 2), indicating that the back side portal also functions as the water channel in FABP3. However, vigorous exchange of water molecules in the gap region was also indicated by the Ratio_NWater values of E72 OE1/OE2 in the apo form (~76%). These results suggest that the widened gap could function as an exit pathway for the internal water molecules when an LCFA ligand enters the binding site through the portal (Figure 10). The gap opening was observed during the PLM binding process in a simulation study of toad Lb-FABP, although Lb-FABP and FABP3 belong to different subfamilies.⁴⁴ The presence of two water-exchange pathways, the back side portal and the open gap, would provide efficient LCFA loading into FABP3 by enhancing discharge of internal water.

In addition, the fully open FABP3 conformation offers a reasonable structure for capturing hydrophobic molecules. The hydrophobic surfaces of the α II and C-D/E-F loops are exposed to the bulk solvent in the fully_open_form and can easily adsorb hydrophobic ligands, including LCFA. Furthermore, the hydrophobicity of the exposed surface of FABP3 may facilitate interactions with plasma membranes, where FABP3 loads LCFA into the binding pocket through the collision-mediated LCFA transfer mechanism.⁸⁰ Efficient binding of ligands in the fully open conformation should be important for the biological function of FABP3, because the protein is highly expressed in cells of high energy-demanding organs such as skeletal and heart muscles. In cells, cytosolic LCFA transport via FABP3 is essential for efficient energy production via mitochondrial β -oxidation of LCFA.^{8,11}

In contrast to the apo form, which primarily showed the wide-open structure, the STE-bound form retained the closed conformation throughout the simulations. This conformational stability is achieved by hydrophobic contact between the portal and bound ligand molecules, and by the stable H-bond networks formed inside the cavity. The present results imply that the release of bound FA from FABP3 seldom occurs in the aqueous environment at 310 K and is controlled by protein–membrane interactions^{3,9,80,81} or protein–protein interactions with other lipid binding protein such as peroxisome proliferator-activator receptor α (PPAR α).^{11,82} Revealing the stabilization mechanism of the open conformation of holo FABP3 will further illuminate the mechanisms underlying targeted FA delivery in cells.

5. CONCLUSION

Using 210 ns MD simulations, we demonstrated that FABP3 predominantly adopts the open conformation at 310 K in the absence of the FA ligand, in which both the portal and gap regions are wide open. Portal opening was triggered by the lack of intermolecular hydrophobic interactions between FABP3 and the FA, and by the increased mobility of internal water molecules in an entropy-driven manner. Gap opening occurred following portal opening, caused by the disorder of the internal water molecules, and especially by destabilization of the H-bond networks around the gap. Portal opening is essential for LCFA to access the internal binding site, and further opening of the gap region is expected to ensure smooth LCFA loading by providing sufficient room for efficient water molecule exit. This would be closely related to the cellular role of FABP3:

efficient transport of LCFA to target organelles, such as mitochondria, for energy production via LCFA β -oxidation.

On the other hand, in the 150 ns MD simulations, STE-bound FABP3 primarily adopted the closed form at 310 K. In the binding cavity of closed FABP3, the internal water molecules formed a stable H-bond network with the highly conserved hydrophilic residues. The gap region was “latched” by the coherent H-bonds formed by the ordered water molecules, and the gap was essentially closed, masking the bound LCFA from the bulk solvent. On the other hand, water molecules around the bound STE had a certain degree of freedom to move synchronously with the bound STE. Along with the hydrophobic interactions between the inner surface of the protein and the bound ligand, water molecules in the binding cavity contribute considerably to holding ligand LCFA in the binding site and to stabilizing the closed form of FABP3.

The present results clearly illustrate the molecular mechanisms of gate opening and stable binding of LCFA by FABP3, involving rearrangement of the H-bond network in the large binding site. The ccHB and interaction dynamics analyses were effective for interpretation of the dynamic behavior of water clusters inside the FABP3 binding cavity, and will provide a versatile strategy for investigation of the role of internal water molecule dynamics in protein stability, protein–ligand recognition, and protein–protein complex formation.

■ ASSOCIATED CONTENT

S Supporting Information

Improvement of the triangulation procedure so that it becomes applicable to a protein in an open form, and simulation detail of the FABP3 in the crystalline environment. Table S1, the additional points used in the triangulation. Table S2, the Ratio_Contact and Ratio_NWater values calculated from the first 25 ns of the trajectories from STE_NPT_run1 and apo_NPT_run1. Table S3, the Ratio_Contact and Ratio_NWater values calculated from the first 25 ns of the trajectories from STE_NPT_run2 and apo_NPT_run2. Figure S1, amino acid sequence comparison of FABP3, FABP4, FABP5, FABP7, and FABP8, and the residues in contact with bound ligand molecules and/or internal water molecules. Figure S2, time courses of the distances between the atoms on α II, C-D/E-F loops, and STE carbon atoms in the simulations STE_NPT_run1 and STE_NPT_run2. Figure S3, time courses of the RMSD values of protein main chain and bound STE from the energy minimized structures and the numbers of internal water molecules in the NVT simulations performed for STE_closed_form, apo_closed_form, and fully_open_form. Figure S4, time courses of the RMSD values for the protein main chain and the bound STE in NVT simulations starting from the protein open structures observed in STE_NPT_run2. Figure S5, comparison of the hydration structures in the binding pocket in the crystal structure and in the MD simulations. Figure S6, RMSF values of protein $C\alpha$ atoms and carbon atoms of bound STE in the simulations STE_closed_form, apo_closed_form, and fully_open_form. Figure S7, illustration of the rearrangement of the H-bond networks in concert with the conformational change of the STE alkyl chain. Figure S8, scatter plots in which horizontal and vertical axes measure Ratio_Contact and Ratio_NWater, respectively. Figure S9, illustration of the structures of FABP3 in the crystalline environment and comparison of the residue-by-residue ASA values of the protein in the solution and crystalline environments. This material is available free of charge via the Internet at <http://pubs.acs.org>.

AUTHOR INFORMATION

Corresponding Author

*E-mail: matsuokas11@chem.sci.osaka-u.ac.jp. Telephone: +81-66850-5845.

Notes

The authors declare no competing financial interest.

ACKNOWLEDGMENTS

We give a special thanks to Prof. Mitsunori Ikeguchi of Yokohama City University for willingly offering MARBLE software and for giving helpful advices for the analyses of the protein under the crystalline environment. We express our gratitude to Dr. Tomotaka Oroguchi of Keio University for graciously teaching D.M. how to use MARBLE software. We are grateful to Drs. Fuminori Sato and Toshiaki Hara for giving their fruitful comments to our study. We also thank Drs. Seiki Baba, Nobuhiro Mizuno and Eiki Yamashita and Prof. Atsushi Nakagawa for their kind help in the data collection at BL38B1 and BL44XU of SPring-8. The synchrotron radiation experiments were performed at SPring-8 with the approval of the Japan Synchrotron Radiation Research Institute (JASRI) (proposal nos. 2012A/B6724, 2012A1370, and 2012B1295). This work was supported in part by JSPS KAKENHI (Japan) Grants 24681045 (S.Ma), 26560436 (S.Ma), 25286051 (S.S.), and 25242073 (M.M.).

REFERENCES

- (1) Veerkamp, J. H.; Peeters, R. A.; Maatman, R. G. H. J. Structural and Functional Features of Different Types of Cytoplasmic Fatty Acid-Binding Proteins. *Biochim. Biophys. Acta* **1991**, *1081*, 1–24.
- (2) Banaszak, L.; Winter, N.; Xu, Z.; Bernlohr, D. A.; Cowan, S.; Jones, T. A. Lipid-Binding Proteins: a Family of Fatty Acid and Retinoid Transport Proteins. *Adv. Protein Chem.* **1994**, *45*, 89–151.
- (3) Glatz, J. F. C.; van der Vusse, G. J. Cellular Fatty Acid-Binding Proteins: Their Function and Physiological Significance. *Prog. Lipid Res.* **1996**, *35*, 243–282.
- (4) Hohoff, C.; Spener, F. Fatty Acid Binding Proteins and Mammary-Derived Growth Inhibitor. *Fett/Lipid* **1998**, *100*, 252–263.
- (5) Lücke, C.; Gutiérrez-González, L. H.; Hamilton, J. A. Intracellular Lipid Binding Proteins: Evolution, Structure, and Ligand Binding. In *Cellular Proteins and their Fatty Acids in Health and Disease*; Duttaroy, A. K., Spener, F., Eds.; Wiley-VCH Verlag GmbH & Co. KGaA: Weinheim, 2003; pp 95–118.
- (6) Haunerland, N. H.; Spener, F. Fatty Acid-Binding Proteins—Insights from Genetic Manipulations. *Prog. Lipid Res.* **2004**, *43*, 328–349.
- (7) Furuhashi, M.; Hotamisligil, G. S. Fatty Acid-Binding Proteins: Role in Metabolic Diseases and Potential as Drug Targets. *Nat. Rev. Drug Discovery* **2008**, *7*, 489–503.
- (8) Glatz, J. F. C.; Paulussen, R. J. A.; Veerkamp, J. H. Fatty Acid Binding Proteins from Heart. *Chem. Phys. Lipids* **1985**, *38*, 115–129.
- (9) Storch, J.; Thumser, A. E. A. The Fatty Acid Transport Function of Fatty Acid-Binding Proteins. *Biochim. Biophys. Acta* **2000**, *1486*, 28–44.
- (10) Hertzel, A. V.; Bernlohr, D. A. The Mammalian Fatty Acid-binding Protein Multigene Family: Molecular and Genetic Insights into Function. *Trends Endocrin. Met.* **2000**, *11*, 175–180.
- (11) Storch, J.; Thumser, A. E. Tissue-Specific Functions in the Fatty Acid-binding Protein Family. *J. Biol. Chem.* **2010**, *285*, 32679–32683.
- (12) Zanotti, G.; Scapin, G.; Spadon, P.; Veerkamp, J. H.; Sacchettini, J. C. Three-Dimensional Structure of Recombinant Human Muscle Fatty Acid-binding Protein. *J. Biol. Chem.* **1992**, *267*, 18541–18550.
- (13) Young, A. C. M.; Scapin, G.; Kromminga, A.; Patel, S. B.; Veerkamp, J. H.; Sacchettini, J. C. Structural Studies on Human Muscle Fatty Acid Binding Protein at 1.4 Å Resolution: Binding Interactions with Three C18 Fatty Acids. *Structure* **1994**, *2*, 523–534.
- (14) Scapin, G.; Young, A. C. M.; Kromminga, A.; Veerkamp, J. H.; Gordon, J. I.; Sacchettini, J. C. High Resolution X-ray Studies of Mammalian Intestinal and Muscle Fatty Acid-Binding Proteins Provide an Opportunity for Defining the Chemical Nature of Fatty Acid: Protein Interactions. *Mol. Cell. Biochem.* **1993**, *123*, 3–13.
- (15) Hirose, M.; Sugiyama, S.; Ishida, H.; Niizuma, M.; Matsuoka, D.; Hara, T.; Mizohata, E.; Murakami, S.; Inoue, T.; Matsuoka, S.; Murata, M. Structure of the Human-Heart Fatty-Acid-Binding Protein 3 in Complex with the Fluorescent Probe 1-Anilinonaphthalene-8-Sulphonic Acid. *J. Synchrotron Radiat.* **2013**, *20*, 923–928.
- (16) Lassen, D.; Lücke, C.; Kveder, M.; Mesgarzadeh, A.; Schmidt, J. M.; Specht, B.; Lezius, A.; Spener, F.; Rüterjans, H. Three-Dimensional Structure of Bovine Heart Fatty-Acid-Binding Protein with Bound Palmitic Acid, Determined by Multidimensional NMR Spectroscopy. *Eur. J. Biochem.* **1995**, *230*, 266–280.
- (17) Woolf, T. B. Simulations of Fatty Acid-Binding Proteins Suggest Sites Important for Function. I. Stearic Acid. *Biophys. J.* **1998**, *74*, 681–693.
- (18) Schaap, F. G.; van der Vusse, G. J.; Glatz, J. F. C. Evolution of the Family of Intracellular Lipid Binding Proteins in Vertebrates. *Mol. Cell. Biochem.* **2002**, *239*, 69–77.
- (19) Balendiran, G. K.; Schnütgen, F.; Scapin, G.; Börchers, T.; Xhong, N.; Lim, K.; Godbout, R.; Spener, F.; Sacchettini, J. C. Crystal Structure and Thermodynamic Analysis of Human Brain Fatty Acid-Binding Protein. *J. Biol. Chem.* **2000**, *275*, 27045–27054.
- (20) Marr, E.; Tardie, M.; Carty, M.; Philips, T. B.; Wang, I.-K.; Soeller, W.; Qiu, X.; Karam, G. Expression, Purification, Crystallization and Structure of Human Adipocyte Lipid-Binding Protein (aP2). *Acta Crystallogr. F* **2006**, *62*, 1058–1060.
- (21) Hohoff, C.; Börchers, T.; Rüstow, B.; Spener, F.; van Tilbeurgh, H. Expression, Purification, and Crystal Structure Determination of Recombinant Human Epidermal-Type Fatty Acid Binding Protein. *Biochemistry* **1999**, *38*, 12229–12239.
- (22) Ruskamo, S.; Yadav, R. P.; Sharma, S.; Lehtimäki, M.; Laulumaa, S.; Aggarwal, S.; Simons, M.; Bürck, J.; Ulrich, A. S.; Juffer, A. H.; Kursula, I.; Kursula, P. Atomic Resolution View Into the Structure-Function Relationships of the Human Myelin Peripheral Membrane Protein P2. *Acta Crystallogr. D* **2014**, *70*, 165–176.
- (23) Lücke, C.; Huang, S.; Rademacher, M.; Rüterjans, H. New Insights into Intracellular Lipid Binding Proteins: The Role of Buried Water. *Protein Sci.* **2002**, *11*, 2383–2392.
- (24) Chaplin, M. Do We Underestimate the Importance of Water in Cell Biology? *Nat. Rev. Mol. Cell Biol.* **2006**, *7*, 861–866.
- (25) Ball, P. Water as an Active Constituent in Cell Biology. *Chem. Rev.* **2008**, *108*, 74–108.
- (26) Williams, M. A.; Goodfellow, J. M.; Thornton, J. M. Buried Waters and Internal Cavities in Monomeric Proteins. *Protein Sci.* **1994**, *3*, 1224–1235.
- (27) Bhat, T. N.; Bentley, G. A.; Boulot, G.; Greene, M. I.; Tello, D.; Dall'Acqua, W.; Souchon, H.; Schwarz, F. P.; Mariuzza, R. A.; Poljak, R. J. Bound Water Molecules and Conformational Stabilization Help Mediate an Antigen-Antibody Association. *Proc. Natl. Acad. Sci. U.S.A.* **1994**, *91*, 1089–1093.
- (28) Takano, K.; Yamagata, Y.; Funahashi, J.; Hioki, Y.; Kuramitsu, S.; Yutani, K. Contribution of Intra- and Intermolecular Hydrogen Bonds to the Conformational Stability of Human Lysozyme. *Biochemistry* **1999**, *38*, 12698–12708.
- (29) Ricchiuto, P.; Rocco, A. G.; Gianazza, E.; Corradini, D.; Beringhelli, T.; Eberini, I. Structural and Dynamic Roles of Permanent Water Molecules in Ligand Molecular Recognition by Chicken Liver Bile Acid Binding Protein. *J. Mol. Recognit.* **2008**, *21*, 348–354.
- (30) Gillilan, R. E.; Ayers, S. D.; Noy, N. Structural Basis for Activation of Fatty Acid-Binding Protein 4. *J. Mol. Biol.* **2007**, *372*, 1246–1260.
- (31) Ory, J. J.; Banaszak, L. J. Studies of the Ligand Binding Reaction of Adipocyte Lipid Binding Protein Using the Fluorescent Probe 1,8-Anilinonaphthalene-8-Sulfonate. *Biophys. J.* **1999**, *77*, 1107–1116.

- (32) Lehmann, F.; Haile, S.; Axen, E.; Medina, C.; Uppenberg, J.; Svensson, S.; Lundbäck, T.; Rondahl, L.; Barf, T. Discovery of Inhibitors of Human Adipocyte Fatty Acid-Binding Protein, a Potential Type 2 Diabetes Target. *Bioorg. Med. Chem. Lett.* **2004**, *14*, 4445–4448.
- (33) Barf, T.; Lehmann, F.; Hammer, K.; Haile, S.; Axen, E.; Medina, C.; Uppenberg, J.; Svensson, S.; Rondahl, L.; Lundbäck, T. N-Benzyl-Indolo Carboxylic Acids: Design and Synthesis of Potent and Selective Adipocyte Fatty-Acid Binding Protein (A-FABP) Inhibitors. *Bioorg. Med. Chem. Lett.* **2009**, *19*, 1745–1748.
- (34) Xu, Z.; Bernlohr, D. A.; Banaszak, L. J. The Adipocyte Lipid-Binding Protein at 1.6-Å Resolution. Crystal Structures of the Apoprotein and with Bound Saturated and Unsaturated Fatty Acids. *J. Biol. Chem.* **1993**, *268*, 7874–7884.
- (35) Armstrong, E. H.; Goswami, D.; Griffin, P. R.; Noy, N.; Ortlund, E. A. Structural Basis for Ligand Regulation of the Fatty Acid-binding Protein 5, Peroxisome Proliferator-Activated Receptor β/δ (FABP5-PPAR β/δ) Signaling Pathway. *J. Biol. Chem.* **2014**, *289*, 14941–14954.
- (36) Ragona, L.; Paganò, K.; Tomaselli, S.; Favretto, F.; Cecon, A.; Zanzoni, S.; D’Onofrio, M.; Assfalg, M.; Molinari, H. The Role of Dynamics in Modulating Ligand Exchange in Intracellular Lipid Binding Proteins. *Biochim. Biophys. Acta* **2014**, *1844*, 1268–1278.
- (37) Sacchettini, J. C.; Scapin, G.; Gopaul, D.; Gordon, J. I. Refinement of the Structure of *Escherichia coli*-Derived Rat Intestinal Fatty Acid Binding Protein with Bound Oleate to 1.75-Å Resolution. Correlation with the Structures of the Apoprotein and the Protein with Bound Palmitate. *J. Biol. Chem.* **1992**, *267*, 23534–23545.
- (38) Constantine, K. L.; Friedrichs, M. S.; Wittekind, M.; Jamil, H.; Chu, C.-H.; Parker, R. A.; Goldfarb, V.; Mueller, L.; Farmer, B. T., II Backbone and Side Chain Dynamics of Uncomplexed Human Adipocyte and Muscle Fatty Acid-Binding Proteins. *Biochemistry* **1998**, *37*, 7965–7980.
- (39) Reese-Wagoner, A.; Thompson, J.; Banaszak, L. Structural Properties of the Adipocyte Lipid Binding Protein. *Biochim. Biophys. Acta* **1999**, *1441*, 106–116.
- (40) Jenkins, A. E.; Hockenberry, J. A.; Nguyen, T.; Bernlohr, D. A. Testing of the Portal Hypothesis: Analysis of a V32G, F57G, K58G Mutant of the Fatty Acid Binding Protein of the Murine Adipocyte. *Biochemistry* **2002**, *41*, 2022–2027.
- (41) Friedman, R.; Nachliel, E.; Gutman, M. Molecular Dynamics Simulations of the Adipocyte Lipid Binding Protein Reveal a Novel Entry Site for the Ligand. *Biochemistry* **2005**, *44*, 4275–4283.
- (42) Friedman, R.; Nachliel, E.; Gutman, M. Fatty Acid Binding Proteins: Same Structure but Different Binding Mechanisms? Molecular Dynamics Simulations of Intestinal Fatty Acid Binding Protein. *Biophys. J.* **2006**, *90*, 1535–1545.
- (43) Tsafadia, Y.; Friedman, R.; Kadmon, J.; Selzer, A.; Nachiel, E.; Gutman, M. Molecular Dynamics Simulations of Palmitate Entry into the Hydrophobic Pocket of the Fatty Acid Binding Protein. *FEBS Lett.* **2007**, *581*, 1243–1247.
- (44) Di Pietro, S. M.; Cársico, B.; Perduca, M.; Monaco, H. L.; Santomé, J. A. Structural and Biochemical Characterization of Toad Liver Basic Fatty Acid-Binding Protein. *Biochemistry* **2003**, *42*, 8192–8203.
- (45) Lücke, C.; Fushman, D.; Ludwig, C.; Hamilton, J. A.; Sacchettini, J. C.; Rütherjans, H. A Comparative Study of the Backbone Dynamics of Two Closely Related Lipid Binding Proteins: Bovine Heart Fatty Acid Binding Protein and Porcine Ileal Lipid Binding Protein. *Mol. Cell. Biochem.* **1999**, *192*, 109–121.
- (46) Zamarreño, F.; Herrera, F. E.; Cársico, B.; Costabel, M. D. Similar Structures but Different Mechanisms. Prediction of FABPs-Membrane Interaction by Electrostatic Calculation. *Biochim. Biophys. Acta* **2012**, *1818*, 1691–1697.
- (47) Ferrolino, M. C.; Zhuravleva, A.; Budyak, I. L.; Krishnan, B.; Gierasch, L. M. Delicate Balance between Functionally Required Flexibility and Aggregation Risk in a β -Rich Protein. *Biochemistry* **2013**, *52*, 8843–8854.
- (48) Woolf, T. B.; Grossfield, A.; Tychko, M. Differences Between Apo and Three Holo Forms of the Intestinal Fatty Acid Binding Protein Seen by Molecular Dynamics Computer Calculations. *Biophys. J.* **2000**, *78*, 608–625.
- (49) Bakowies, D.; van Gunsteren, W. F. Simulations of Apo and Holo-Fatty Acid Binding Protein: Structure and Dynamics of Protein, Ligand and Internal Water. *J. Mol. Biol.* **2002**, *315*, 713–736.
- (50) Søndergaard, C. R.; Olsson, M. H. M.; Rostkowski, M.; Jensen, J. H. Improved Treatment of Ligands and Coupling Effects in Empirical Calculation and Rationalization of pK_a values. *J. Chem. Theory Comput.* **2011**, *7*, 2284–2295.
- (51) Ikeguchi, M. Partial Rigid-Body Dynamics in NPT, NPAT and $N\bar{\gamma}T$ Ensembles for Protein and Membranes. *J. Comput. Chem.* **2004**, *25*, 259–259.
- (52) Best, R. B.; Zhu, X.; Shim, J.; Lopes, P. E. M.; Mittal, J.; Feig, M.; MacKerell, A. D., Jr. Optimization of the Additive CHARMM All-Atom Protein Force Field Targeting Improved Sampling of the Backbone ϕ , ψ and Side-Chain χ_1 and χ_2 Dihedral Angles. *J. Chem. Theory Comput.* **2012**, *8*, 3257–3273.
- (53) Klauda, J. B.; Venable, R. M.; Freites, J. A.; O’Connor, J. W.; Tobias, D. J.; Mondragon-Ramirez, C.; Vorobyov, I.; MacKerell, A. D., Jr.; Pastor, R. W. Update of the CHARMM All-Atom Additive Force Field for Lipids: Validation on Six Lipid Types. *J. Phys. Chem. B* **2010**, *114*, 7830–7843.
- (54) Jorgensen, W. L.; Chandrasekhar, J.; Madura, J. D.; Impey, R. W.; Klein, M. L. Comparison of Simple Potential Functions for Simulating Liquid Water. *J. Chem. Phys.* **1983**, *79*, 926–935.
- (55) Marthyra, G. J.; Tobias, D. J.; Klein, M. L. Constant Pressure Molecular Dynamics Algorithms. *J. Chem. Phys.* **1994**, *101*, 4177–4189.
- (56) Lee, B.; Richards, F. M. The Interpretation of Protein Structures: Estimation of Static Accessibility. *J. Mol. Biol.* **1971**, *55*, 379–400.
- (57) Kabsch, W. A Solution for the Best Rotation to Relate Two Sets of Vectors. *Acta Crystallogr. A* **1976**, *32*, 922–923.
- (58) Kabsch, W. A Discussion of the Solution for the Best Rotation to Relate Two Sets of Vectors. *Acta Crystallogr. A* **1978**, *34*, 827–828.
- (59) Matsuoka, D.; Nakasako, M. Prediction of Hydration Structures around Hydrophilic Surfaces of Proteins by Using the Empirical Hydration Distribution Functions from a Database Analysis. *J. Phys. Chem. B* **2010**, *114*, 4652–4663.
- (60) Finney, J. L. Water? What’s So Special about It? *Philos. Trans. R. Soc. London B* **2004**, *359*, 1145–1165.
- (61) Matsuoka, D.; Nakasako, M. Probability Distributions of Hydration Water Molecules around Polar Protein Atoms Obtained by a Database Analysis. *J. Phys. Chem. B* **2009**, *113*, 11274–11292.
- (62) Bakowies, D.; van Gunsteren, W. F. Water in Protein Cavities: A Procedure to Identify Internal Water and Exchange Pathways and Application to Fatty Acid-Binding Protein. *Proteins: Struct., Funct., Bioinf.* **2002**, *47*, 534–545.
- (63) Lounnas, V.; Pettitt, B. M. A Connected-Cluster of Hydration around Myoglobin: Correlation between Molecular Dynamics Simulations and Experiment. *Proteins: Struct., Funct., Genet.* **1994**, *18*, 133–147.
- (64) Higo, J.; Nakasako, M. Hydration Structure of Human Lysozyme Investigated by Molecular Dynamics Simulation and Cryogenic X-ray Crystal Structure Analyses: on the Correlation between and Crystal Water Sites, Solvent Density and Solvent Dipole. *J. Comput. Chem.* **2002**, *23*, 1323–1336.
- (65) Yokomizo, T.; Nakasako, M.; Yamazaki, T.; Shindo, H.; Higo, J. Hydrogen-Bond Patterns in the Hydration Structure of a Protein. *Chem. Phys. Lett.* **2005**, *401*, 332–336.
- (66) Yokomizo, T.; Higo, J.; Nakasako, M. Patterns and Networks of Hydrogen-Bonds in the Hydration Structure of Human Lysozyme. *Chem. Phys. Lett.* **2005**, *410*, 31–35.
- (67) Hodsdon, M. E.; Cistola, D. P. Discrete Backbone Disorder in the Nuclear Magnetic Resonance Structure of Apo Intestinal Fatty Acid-Binding Protein: Implications for the Mechanism of Ligand Entry. *Biochemistry* **1997**, *36*, 1450–1460.
- (68) Lu, J.; Lin, C.-L.; Tang, C.; Ponder, J. W.; Kao, J. L. F.; Cistola, D. P.; Li, E. Binding of Retinol Induces Changes in Rat Cellular

- Retinol-binding Protein II Conformation and Backbone Dynamics. *J. Mol. Biol.* **2000**, *300*, 619–632.
- (69) Franzoni, L.; Lücke, C.; Pérez, C.; Cavazzini, D.; Rademacher, M.; Ludwig, C.; Spisni, A.; Rossi, G. L.; Rüterjans, H. Structure and Backbone Dynamics of Apo- and Holo-cellular Retinol-binding Protein in Solution. *J. Biol. Chem.* **2002**, *277*, 21983–21997.
- (70) Otting, G.; Liepinsh, E.; Wüthrich, K. Protein Hydration in Aqueous Solution. *Science* **1991**, *254*, 974–980.
- (71) Denisov, V. P.; Halle, B. Protein Hydration Dynamics in Aqueous Solution. *Faraday Discuss.* **1996**, *103*, 227–244.
- (72) Halle, B. Protein Hydration Dynamics in Solution: a Critical Survey. *Philos. Trans. R. Soc. London B* **2004**, *359*, 1207–1224.
- (73) Sinha, S. K.; Bandyopadhyay, S. Dynamic Properties of Water around a Protein-DNA Complex from Molecular Dynamics Simulations. *J. Chem. Phys.* **2011**, *135*, 135101.
- (74) Kohn, J. E.; Afonine, P. V.; Ruscio, J. Z.; Adams, P. D.; Head-Gordon, T. Evidence of Functional Protein Dynamics from X-ray Crystallographic Ensembles. *PLoS Comput. Biol.* **2010**, *6*, e1000911.
- (75) Garman, E. ‘Cool’ Crystals: Macromolecular Cryocrystallography and Radiation Damage. *Curr. Opin. Struct. Biol.* **2003**, *13*, 545–551.
- (76) Halle, B. Biomolecular Cryocrystallography: Structural Changes during Flash-Cooling. *Proc. Natl. Acad. Sci. U.S.A.* **2004**, *101*, 4793–4798.
- (77) Friedmann, R.; Caflisch, A. On the Orientation of the Catalytic Dyad in Aspartic Proteases. *Proteins* **2010**, *78*, 1575–1582.
- (78) D’Onofrio, M.; Ragona, L.; Fessas, D.; Signorelli, M.; Ugolini, R.; Pedò, M.; Assfalg, M.; Molinari, H. NMR Unfolding Studies on a Liver Bile Acid Binding Protein Reveal a Global Two-State Unfolding and Localized Singular Behaviors. *Arch. Biochem. Biophys.* **2009**, *481*, 21–29.
- (79) Zimmerman, A. W.; Rademacher, M.; Rüterjans, H.; Lücke, C.; Veerkamp, J. H. Functional and Conformational Characterization of New Mutants of Heart Fatty Acid-Binding Protein. *Biochem. J.* **1999**, *344*, 495–501.
- (80) Franchini, G. R.; Storch, J.; Corsico, B. The Integrity of the α -Helical Domain of Intestinal Fatty Acid Binding Pocket Is Essential for the Collision-Mediated Transfer of Fatty Acids to Phospholipid Membranes. *Biochim. Biophys. Acta* **2008**, *1781*, 192–199.
- (81) Liou, H.-L.; Kahn, P. C.; Storch, J. Role of the Helical Domain in Fatty Acid Transfer from Adipocyte and Heart Fatty Acid-binding Proteins to Membrane. *J. Biol. Chem.* **2002**, *277*, 1806–1815.
- (82) Tan, N.-S.; Shaw, N. S.; Vinckenbosch, N.; Liu, P.; Yasmin, R.; Desvergne, B.; Wahli, W.; Noy, N. Selective Cooperation between Fatty Acid Binding Proteins and Peroxisome Proliferator-Activated Receptors in Regulating Transcription. *Mol. Cell. Biol.* **2002**, *22*, 5114–5127.